

Estimation of Critical Cooling Rates for Glass Formation in Bulk Metallic Glasses through Non-isothermal Thermal Analysis

Ji-Hun Kim^{1*}, Joon Sik Park¹, Eun Soo Park¹, Won Tae Kim², and Do Hyang Kim¹

¹ Center for Noncrystalline Materials, Department of Metallurgical Engineering, Yonsei University, 134 Sinchon-dong, Seodaemun-gu, Seoul 120-749, Korea

² Applied Science Division, Cheongju University, Naedeok 2-dong, Cheongju 360-764, Korea

Critical cooling rate (R_c) for glass formation has been calculated from an integrated transformation curve, constructed by combining continuous cooling transformation (CCT) and continuous heating transformation (CHT) curves. The CCT and CHT curves were calculated from experimental measurements on cooling rate dependence of solidification onset temperature using classical nucleation kinetics and heating rate dependence of crystallization onset temperature using Kissinger method, respectively. The critical cooling rate was calculated from the intersection point of the two curves, corresponding to an apparent nose point in the integrated transformation curve. The calculated critical cooling rates were in good agreement with those measured for five different bulk glass forming alloys of Ca-Mg-Zn, Pd-Ni-Cu-P, Zr-Ti-Cu-Ni-Be and Mg-Cu-Y alloys.

Keywords: critical cooling rate, glass forming ability, bulk metallic glass

1. INTRODUCTION

An estimation of critical cooling rate for glass formation of metallic glass is useful to design and develop new metallic glass systems having high glass forming ability (GFA). Several thermal parameters have been proposed to reflect GFA [1-3]: reduced glass transition temperature, T_{rg} ($=T_g/T_L$, where T_g and T_L are glass transition and liquidus temperature, respectively); range of supercooled liquid region, ΔT_x ($=T_x - T_g$, where T_x is the onset temperature of crystallization during heating a glass); and parameter γ ($=T_x/(T_g + T_L)$). In general, GFA of an alloy is expected to increase with increasing the magnitude of these parameters [3,4], even though there are some examples showing exceptional cases [5,6]. The GFA can be expressed either by the critical cooling rate (R_c) for glass formation or the maximum-sectioned thickness (Z_c) of bulk metallic glass (BMG) [7-17]. As the GFA increases, R_c decreases and Z_c increases. Therefore, proper estimation of R_c for glass formation of an alloy from thermal analysis data, which can be relatively easily obtained, will be helpful to develop a new alloy system having high GFA. Often the critical cooling rate, R_c^* , for glass formation has been calculated from the variation of solidification onset temperature, T_{xs} , with cooling rate, α , using following equation [9,10];

$$\ln \alpha = \ln R_c^* + \frac{d}{(T_L - T_{xs})^2} \quad (1)$$

where T_L is the liquidus temperature, d is material factor. While the above relationship has been applied in many BMG systems, the estimation based upon Eq. 1 showed a large discrepancy from experimentally measured data, as will be shown in this study.

During solidification process, a liquid phase transformed into either a crystalline phase or into an amorphous phase. Even though the formation of crystalline phase is more favorable from the thermodynamic point of view, the amorphous phase formation can take place if the cooling rate is fast enough to avoid the nucleation and growth of the crystalline phase. If a continuous cooling transformation (CCT) curve of liquid is successfully obtained, the critical cooling rate for glass formation can be calculated from the position of nose point [11,13]. Unfortunately, there is a difficulty in building a complete CCT curve across the whole temperature range between liquidus and glass transition temperature, especially below the nose temperature due to the experimental limitations. It has been suggested that the identification of thermal stability of amorphous phase during continuous heating transformation (CHT) curve can provide a kinetic boundary between glass and crystalline phase during heating [18]. Therefore integrated transformation curve, providing a global kinetic boundary between glass and crystalline phase in the entire temperature range between liquidus and glass

*Corresponding author: kjhappy@yonsei.ac.kr

transition temperature can be constructed by combining CCT and CHT curves, which are meaningful above and below a nose temperature, respectively.

In this study, a new method to estimate the critical cooling rate, R_c , for glass formation has been developed by building an integrated transformation curve, which is constructed by combining CCT and CHT curves. We have calculated the CCT and CHT curves from experimental measurements of cooling rate dependence of solidification onset temperature using classical nucleation kinetics and heating rate dependence of crystallization onset temperature by extension of Kissinger method, respectively. The critical cooling rate was estimated from the intersection point of the two curves, corresponding to the apparent nose point of the integrated transformation curve. The calculated values of R_c exhibited a close match to those of experimental measurements in selected Ca-Mg-Zn, Pd-Ni-Cu-P, Vit1, Vit1a and Mg-Cu-Y alloys [5,6,14,20-23].

2. EXPERIMENTAL PROCEDURE

The model predicting the critical cooling rate for glass formation was applied to five different alloys with compositions of $\text{Ca}_{65}\text{Mg}_{15}\text{Zn}_{20}$, $\text{Pd}_{40}\text{Ni}_{10}\text{Cu}_{30}\text{P}_{20}$, $\text{Zr}_{41.2}\text{Ti}_{13.8}\text{Cu}_{12.5}\text{Ni}_{10}\text{Be}_{22.5}$ (Vit1), $\text{Zr}_{42.6}\text{Ti}_{12.4}\text{Cu}_{11.3}\text{Ni}_{10}\text{Be}_{23.8}$ (Vit1a) and $\text{Mg}_{65}\text{Cu}_{25}\text{Y}_{10}$. These alloys were selected because they show different ranges of critical cooling rates from 0.1 to about ~ 100 K/s [1,4]. $\text{Ca}_{65}\text{Mg}_{15}\text{Zn}_{20}$ and $\text{Mg}_{65}\text{Cu}_{25}\text{Y}_{10}$ alloys were prepared by induction melting high purity elements (99.9 %) in BN coated graphite crucibles under an Ar atmosphere, followed by casting the liquid into a cone-shaped copper mold with dimensions of 6 mm in diameter at the bottom, 15 mm in diameter at the top and 45 mm in height. For direct measurements of R_c , variations of temperature with time were monitored during solidification of $\text{Ca}_{65}\text{Mg}_{15}\text{Zn}_{20}$ at three central positions with different heights by using inserted thermocouples. $\text{Zr}_{41.2}\text{Ti}_{13.8}\text{Cu}_{12.5}\text{Ni}_{10}\text{Be}_{22.5}$ (Vit1) alloy ingot has been prepared by arc-melting elemental components and Be-Cu-Ni alloys in a purified atmosphere. To fabricate the BMG a self-designed plate-shaping equipment was used: after melting of the ingot by arc in an Ar atmosphere, the melt was sandwiched immediately between two water-chilled copper rod, resulting that a circular coupon was obtained with a dimension of about 4 mm in thickness and 5 cm in diameter. Commercial Vit1a BMG in a sheet form with a thickness of 4 mm was obtained from Liquid Metal® in Korea. For the $\text{Pd}_{40}\text{Ni}_{10}\text{Cu}_{30}\text{P}_{20}$ alloy, the ingot was prepared by arc-melting a mixture of pure metallic elements (purity 99.9~99.99 %) and pre-alloyed $\text{Pd}_{60}\text{P}_{40}$ in a purified argon atmosphere. The ingot was sealed in a quartz tube under high vacuum, heated above the liquidus temperature, and then quenched in water. Details of the preparation procedure of the bulk $\text{Pd}_{40}\text{Ni}_{10}\text{Cu}_{20}\text{P}_{20}$ alloy sample have been reported elsewhere [14,20].

Rapid solidification of the alloys was performed by using melt spinning technique with a surface velocity of Cu wheel of 40 m/s. The amorphous nature and presence of crystalline phases were identified by X-ray diffractometry (XRD (Rigaku CN-2301 X-ray diffractometer)). The thermal properties (T_g , T_x) of melt spun ribbons and BMGs were measured at various heating rates between 0.083 and 1.334 K/s by differential scanning calorimetry (DSC (Perkin-Elmer DSC7)). Melting and solidification behavior of the specimens was monitored using differential thermal analyses experiments (DTA (Perkin-Elmer DTA7)). The liquidus temperature was assumed to be the end point of endothermic peak obtained during continuous heating with a heating rate of 0.667 K/s. The onset temperature of solidification (T_{sx}) during cooling was measured at various cooling rates between 0.03 and 0.5 K/s.

3. RESULTS AND DISCUSSION

3.1. Thermal properties

Fig. 1 shows DSC traces obtained from melt spun ribbon samples during continuous heating with a heating rate of 0.667 K/s. The $\text{Ca}_{65}\text{Mg}_{15}\text{Zn}_{20}$, $\text{Pd}_{40}\text{Ni}_{10}\text{Cu}_{30}\text{P}_{20}$, $\text{Zr}_{41.2}\text{Ti}_{13.8}\text{Cu}_{12.5}\text{Ni}_{10}\text{Be}_{22.5}$, $\text{Zr}_{42.6}\text{Ti}_{12.4}\text{Cu}_{11.3}\text{Ni}_{10}\text{Be}_{23.8}$ and $\text{Mg}_{65}\text{Cu}_{25}\text{Y}_{10}$ alloy samples exhibited large supercooled liquid regions (ΔT_x) of 27, 88, 67, 97, and 68 K, respectively, with subsequent sharp exothermic peaks of the crystallization events at the onset temperatures (T_c) of 408, 665, 715, 735, and 494 K, respectively. The sharp endothermic peak at high temperature region for the $\text{Ca}_{65}\text{Mg}_{15}\text{Zn}_{20}$ alloy (Fig. 1(a)) corresponds to the melting event of the eutectic solid, which was formed during the continuous heating. The measured T_g and T_x values at various heating rates are listed in Table 1 together with previously reported data for comparison. As can be noticed the mea-

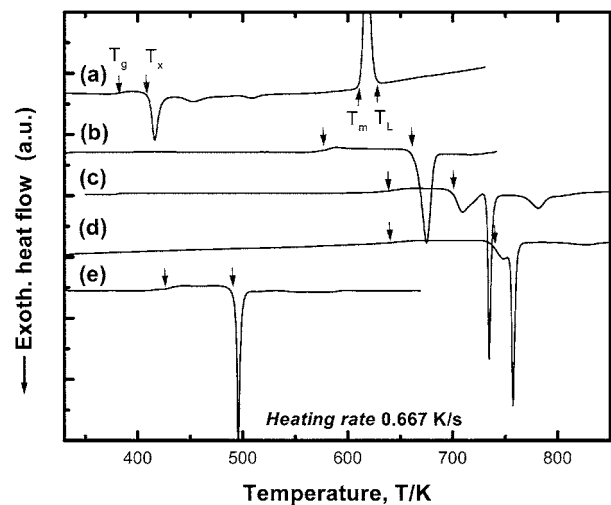


Fig. 1. DSC traces taken from melt spun ribbon alloy samples on continuous heating at a heating rate of 0.667 K/s: (a) $\text{Ca}_{65}\text{Mg}_{15}\text{Zn}_{20}$ alloy, (b) $\text{Pd}_{40}\text{Ni}_{10}\text{Cu}_{30}\text{P}_{20}$ alloy, (c) $\text{Zr}_{41.2}\text{Ti}_{13.8}\text{Cu}_{12.5}\text{Ni}_{10}\text{Be}_{22.5}$, (d) $\text{Zr}_{42.6}\text{Ti}_{12.4}\text{Cu}_{11.3}\text{Ni}_{10}\text{Be}_{23.8}$ alloy, and (e) $\text{Mg}_{65}\text{Cu}_{25}\text{Y}_{10}$ alloy.

Table 1. Intercept values (c) and slopes ($-E/R$) in the plot of $\ln(\beta/T_x^2)$ versus $1/T_x$ derived by Eq. 6 together with data of the glass transition temperatures (T_g) and onset temperatures of crystallization (T_x) for investigate alloys

Alloy (Nominal at.%)	Heating rate (K/s)	T_g (K)	T_x (K)	c	$-E/R \times 10^3$
Ca ₆₅ Mg ₁₅ Zn ₂₀	1.334	388.4	414	24.3	14.9
	0.667	380.6	407.4		
	0.333	371.8	399.6		
	0.167	365.0	392.4		
	0.083	360.2	386.3		
	0.667 [4]	379	412		
Pd ₄₀ Ni ₁₀ Cu ₃₀ P ₂₀	1.334	582.1	675.9	32.6	30.6
	0.667	577.7	665.2		
	0.333	574.2	655.7		
	0.167	570.8	647.5		
	0.333 [1]	576.9	655.8		
Zr _{41.2} Ti _{13.8} Cu _{12.5} Ni ₁₀ Be _{22.5} (Vit1)	1.334	659	740	9.01	16.2
	0.667	648	715		
	0.333	641	698		
	0.167	631	680		
	0.167 [6]*	623	672		
Zr _{42.6} Ti _{12.4} Cu _{11.3} Ni ₁₀ Be _{23.8} (Vit1a)	1.334	645.5	778.3	3.52	12.8
	0.667	638.5	735.0		
	0.333	635	718.3		
	0.167	622.6	699.6		
	0.167 [6]*	623	712		
Mg ₆₅ Cu ₂₅ Y ₁₀	0.833	429.2	499.4	19.9	16.2
	0.667	426	494.0		
	0.500	423	491.1		
	0.333	420.6	485.0		
	0.167	418.8	475.5		
	0.083	417.6	467.6		
	0.667 [22]	420	490		

Data of T_x and T_g were obtained by DSC in the range of heating rate from 1.334 to 0.083 K/s.

*The data were obtained by DTA at a heating rate of 0.167 K/s [6].

sured data in this study were similar to the previously reported corresponding values [1,5,7,23]. As the heating rate increases, both T_g and T_x increase. Supercooled liquid region (ΔT_x) increases with heating rate for Pd₄₀Ni₁₀Cu₃₀P₂₀, Vit1, Vit1a and Mg₆₅Cu₂₅Y₁₀ alloys, while ΔT_x for Ca₆₅Mg₁₅Zn₂₀ is independent of heating rate. The abnormal thermal behavior of ΔT_x in Ca₆₅Mg₁₅Zn₂₀ has been reported elsewhere [5].

Cooling rate dependences of solidification onset temperature, corresponding to the onset temperature of primary exothermic peak in DTA trace, were obtained by DTA experiments at various cooling rates. Table 2 lists the liquidus temperatures (T_L) and cooling rate dependences of solidification onset temperature (T_{xs}) for the alloys, time for the onset of solidification (t_1). The time for the onset of solidification was obtained from exothermic heat vs. time curve at various cooling rates. Also reported liquidus temperatures of each alloy were included for comparison. Due to the difference in measurement conditions, there are minor differences between the measured and reported data. The measured liquidus tem-

peratures were higher than the reported data except for Ca₆₅Mg₁₅Zn₂₀ alloy mainly due to higher heating rate adopted in this study (the observed liquidus temperature dependence upon heating rate is well documented elsewhere [24]). Solidification onset temperature decreased significantly with increasing cooling rate for all alloys. For example, T_{xs} of Ca₆₅Mg₁₅Zn₂₀ alloy decreased from 565 to 557 K with increasing cooling rate from 0.083 to 0.667 K/s.

3.2. Estimation of continuous cooling transformation kinetics

At temperature T below melting temperature, the number (N) of nucleation events in melt of volume (V_p) after time t_1 can be expressed by

$$I_{ss}V_p t = N \quad (2)$$

where I_{ss} is the steady state nucleation rate [8,11]. Time t_1 for the first nucleation event, $N=1$, can be expressed as follows

Table 2. Intercept values (a) and slopes (b) in the plot of $\ln t_1$ versus $T_L^2(T+T_L)^2/(T^3\Delta T^2)$ derived by Eq. 5 together with data of the onset temperatures of solidification (T_{xs}) and liquidus temperatures (T_L) for investigated alloys

Alloy (Nominal at.%)	Cooling rate (K/s)	T_{xs} (K)	t_1 (s)	Mean of T_L (K)	a	b	r^*	T_L in reference
Ca ₆₅ Mg ₁₅ Zn ₂₀	0.667	557	102	621.9±2.15	0.99±0.799	5.24±0.96	0.91	624 [4]
	0.583	558.7	113.7					
	0.500	559	132					
	0.417	559.4	157					
	0.333	561	192					
	0.250	562	252					
	0.167	560.5	387					
	0.083	565	565					
Pd ₄₀ Ni ₁₀ Cu ₃₀ P ₂₀	0.368	712	461.8	889.4±7.1	4.71±0.897	10.66±4.02	0.84	836 [1]**
	0.328	706	567.6					
	0.163	722	1079.8					
	0.081	738	1915.9					
	0.041	760.5	2978.2					
Zr _{41.2} Ti _{13.8} Cu _{12.5} Ni ₁₀ Be _{22.5} (Vit1)	0.462	917.7	342.1	1049.3±0.21	4.78±0.47	3.49±1.05	0.92	996 [6]***
	0.328	921.5	494.4					
	0.167	936.1	956.9					
	0.083	961.3	1894.6					
Zr _{42.6} Ti _{12.4} Cu _{11.3} Ni ₁₀ Be _{23.8} (Vit1a)	0.507	923.7	342.1	1099.1±2.39	-3.66±1.230	46.1±5.51	0.99	1057 [6]***
	0.347	927.4	494.4					
	0.169	935.9	956.9					
	0.084	944.1	1894.6					
Mg ₆₅ Cu ₂₅ Y ₁₀	0.404	715.5	162.3	781.1±1.08	1.97±1.15	3.24±0.934	0.90	770.9 [1]**
	0.368	719.6	163.3					
	0.189	728.6	275					
	0.090	730	579.8					
	0.030	733.9	1579.9					

*Correlation coefficient

**Heating rate 0.333 K/s [1]

***Heating rate 0.167 K/s [6]

using classical steady-state heterogeneous nucleation kinetics.

$$\ln t_1 = -\ln(V_p A_v N_s^o v) + \left(\frac{16\pi\sigma^3 f(\theta)}{3k_B T \Delta G^2} \right) \quad (3)$$

where the term $A_v N_s^o v$ is a prefactor in the expression of nucleation frequency (here, A_v is the area of nucleating substrate per unit volume of melt, N_s^o is the number of molecules per unit area of the substrate, v is the frequency of attempts by atom to cross the phase boundary), σ is the interface energy between solid nucleus and liquid, $f(\theta)$ is wetting factor, k_B is Boltzmann constant, and ΔG is Gibbs free energy difference between solid and liquid.

Several models have been proposed to calculate ΔG in an undercooled liquid [25–27]. Mondal *et al.* has pointed out that the driving forces calculated by Thompson and Spaepens model [26] are in good agreement with experimentally measured data in several glass forming alloys such as Au_{81.4}Si_{18.6}, La₅₀Al₃₀Ni₂₀ and Zr_{41.2}Ti_{13.8}Cu_{12.5}Ni₁₀Be_{22.5}, etc. [27]. Therefore, in this estimation, ΔG at temperature T below liquidus temperature T_L was calculated using following equation, cor-

responding to Thompson and Spaepens model.

$$\Delta G(T) = \frac{2\Delta H \Delta T \left(\frac{T}{T_L} \right)}{T_L + T} \quad (4)$$

Here, ΔH is the latent heat of solidification and ΔT is undercooling ($=T_L - T$).

When the estimation of free energy is plugged in Eq. 3 with an assumption of temperature-independent surface energy for simplification, Eq. 3 may be rewritten by

$$\begin{aligned} \ln t_1 &= -\ln(V_p A_v N_s^o v) + \left(\frac{4\pi\sigma^3 f(\theta)}{3k_B \Delta H^2} \right) \left(\frac{T_L^2 (T + T_L)^2}{T^3 \Delta T^2} \right) \\ &= a + b \left(\frac{T_L^2 (T + T_L)^2}{T^3 \Delta T^2} \right) \end{aligned} \quad (5)$$

where a and b are the intercept and slope of the plot $\ln t_1$ versus $T_L^2(T+T_L)^2/(T^3\Delta T^2)$, respectively.

Following previous works [11,13], we determine the transformation kinetics of the undercooled liquid using the measurements of undercooling as a function of cooling rate, as

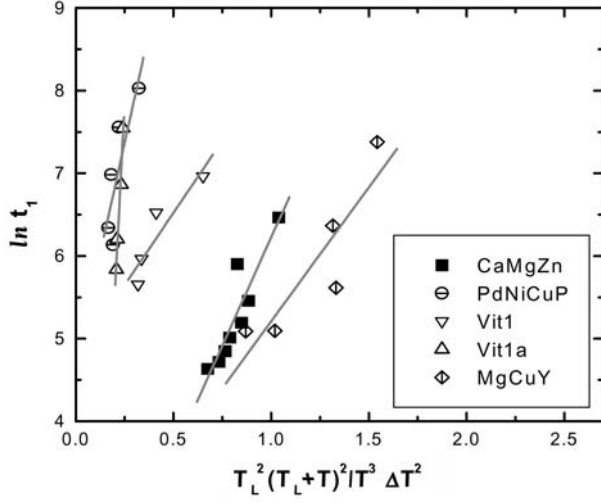


Fig. 2. Plots of $\ln t_1$ versus $T_L^2(T+T_L)^2/(T^3\Delta T^2)$ for amorphous $\text{Ca}_{65}\text{Mg}_{15}\text{Zn}_{20}$, $\text{Pd}_{40}\text{Ni}_{10}\text{Cu}_{30}\text{P}_{20}$, $\text{Zr}_{41.2}\text{Ti}_{13.8}\text{Cu}_{12.5}\text{Ni}_{10}\text{Be}_{22.5}$, $\text{Zr}_{42.6}\text{Ti}_{12.4}\text{Cu}_{11.3}\text{Ni}_{10}\text{Be}_{23.8}$ and $\text{Mg}_{65}\text{Cu}_{25}\text{Y}_{10}$ alloys. Here, T can be substituted by onset temperature of solidification (T_x).

shown in Table 2. Under the assumption of heterogeneous nucleation of constant density, nucleation kinetics plot can be constructed by plotting $\ln t_1$ versus $T_L^2(T+T_L)^2/(T^3\Delta T^2)$. Fig. 2 shows the nucleation kinetics plots for the glassy $\text{Ca}_{65}\text{Mg}_{15}\text{Zn}_{20}$, $\text{Pd}_{40}\text{Ni}_{10}\text{Cu}_{30}\text{P}_{20}$, Vit1, Vit1a and $\text{Mg}_{65}\text{Cu}_{25}\text{Y}_{10}$ alloys. As expected from Eq. 5, there was a linear relationship between $\ln t_1$ versus $T_L^2(T+T_L)^2/(T^3\Delta T^2)$ for all alloys. Through the linear relationship, intercept value a , the slope b , and correlation coefficient (r) can be calculated. As can be noticed, the values of correlation coefficient for these regressions were larger than 0.9 except for the case of $\text{Pd}_{40}\text{Ni}_{10}\text{Cu}_{30}\text{P}_{20}$ alloy, indicating a good linear relationship between $\ln t_1$ and $T_L^2(T+T_L)^2/(T^3\Delta T^2)$. Once the values of a and b are determined, continuous cooling transformation (CCT) curve can be calculated using Eq. 5. It should be noted that the calculated CCT curve is only effective above a certain temperature because temperature dependence of prefactor $A_v N_s^0 v$ in Eq. 3 is ignored. While the assumption is reasonable for the temperature range at not too large undercooling [11], in the vicinity of the glass transition temperature, the prefactor can be overestimated because the temperature dependence of the prefactor is much more pronounced than that of ΔG .

3.3. Continuous heating transformation kinetics

In order to construct CHT curves, an extended analysis of the Kissinger method has been applied [18]. In general, the peak temperature of crystallization (T_p) is used in Kissinger analysis to investigate the maximum transformation rate during crystallization of glass and to reduce the experimental error in temperature measurements by measuring the peak temperature. However, T_p can be substituted by onset temperature of crystallization (T_x) in order to calculate a CHT

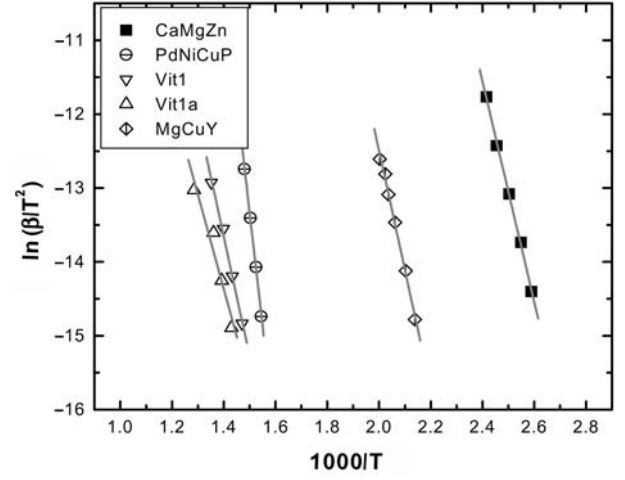


Fig. 3. Plots of $\ln(\beta/T_x^2)$ versus $1/T_x$ on Kissinger analysis for amorphous $\text{Ca}_{65}\text{Mg}_{15}\text{Zn}_{20}$, $\text{Pd}_{40}\text{Ni}_{10}\text{Cu}_{30}\text{P}_{20}$, $\text{Zr}_{41.2}\text{Ti}_{13.8}\text{Cu}_{12.5}\text{Ni}_{10}\text{Be}_{22.5}$, $\text{Zr}_{42.6}\text{Ti}_{12.4}\text{Cu}_{11.3}\text{Ni}_{10}\text{Be}_{23.8}$ and $\text{Mg}_{65}\text{Cu}_{25}\text{Y}_{10}$ alloys.

curve for the devitrification of glass, which indicates an actual starting point (i.e., onset temperature and time) for the transformation from glass to crystalline phase under various heating rates. In this analysis, heating rate dependence of crystallization onset temperature during continuous heating experiments can be expressed as follow [27,28]

$$\ln\left(\frac{\beta}{T_x^2}\right) = \frac{-E}{RT_x} + c \quad (6)$$

where E is the activation energy for nucleation and growth, R is the gas constant and β is the heating rate and c is a constant. From Eq. 6, $\ln(\beta/T_x^2)$ varies linearly with $1/T_x$, with a slope and intercept of $-E/R$ and c , respectively. Fig. 3 shows variations of crystallization onset temperature (T_x) with heating rate (β), re-plotted from Table 1 according to Eq. 6. There was a good linear relationship between $\ln(\beta/T_x^2)$ and $1/T_x$ for all alloys. The values of slope and intercept for each alloy are listed in Table 1. Once the values of slope ($-E/R$) and intercept (c) are determined, continuous heating transformation (CHT) curve of T_x versus heating time ($=(T_x-298)/\beta$) can be calculated using Eq. 6. For a given heating rate, crystallization onset temperature T_x for primary devitrification process can be calculated with this CHT curve. The thermal stability of glass against crystallization is mainly dependent on the required atomic mobility for nucleation and growth of a crystalline phase, especially at the temperature range near T_g and T_x . For the case of linear heating, the lower atomic mobility and its lower temperature dependence suppresses the devitrification of glass, because a larger incubation time and higher temperature are required. Atomic mobility required for crystallization of glass is strongly dependent on the type of devitrification process (e.g., primary, polymorphous and eutectic-type transformation, etc.). In fact, Louzine *et al.* have pointed

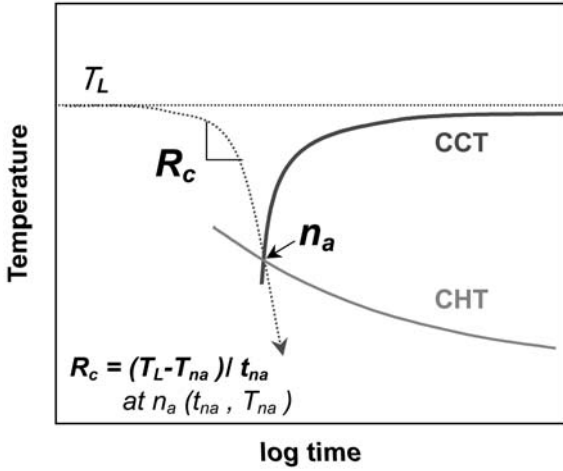


Fig. 4. Schematics of an apparent nose point, n_a , derived as a crossing point of a continuous cooling transformation (CCT) curve with a continuous heating transformation (CHT) curve and a determination of a critical cooling rate for glass formation, R_c , obtained by using n_a .

out that the curvature of CHT curve (i.e., heating rate dependence of crystallization behavior), is closely related to the initial devitrification mechanism of glass [29].

3.4. Integrated transformation kinetics

In order to complete the kinetic boundary of phase transformation from an undercooled liquid to a crystalline solid, the integrated transformation curve has been constructed by combining the CCT and CHT curves. Fig. 4 shows a schematic illustration of the integrated transformation curve. The CCT curve gives a boundary for the onset of crystalline phase formation from liquid. As mentioned previously, however, the CCT curve is effective above a certain temperature due to the ignorance of temperature dependence of prefactor in Eq. 3. At lower temperature region, CHT curve is adopted to give a kinetic boundary between glass formation and crystalline phase formation. The CHT curve corresponds to the onset of crystallization of highly undercooled liquid. Then an integrated transformation curve is constructed by taking the CCT curve at high temperature region and CHT curve at lower temperature region. The CCT and CHT curves intersect at an intermediate temperature, which can be considered as an apparent nose temperature of the integrated transformation curve as shown in Fig. 4. If a cooling curve enters into the domain inside the integrated curve, nucleation of primary crystalline phase occurs and glass formation is not available. Therefore, the critical cooling rate for glass transition can be calculated from the intersection point n_a as follow

$$R_c = \frac{T_L - T_{na}}{t_{na}} \quad (7)$$

where T_{na} and t_{na} represent the temperature and time of the nose point, respectively.

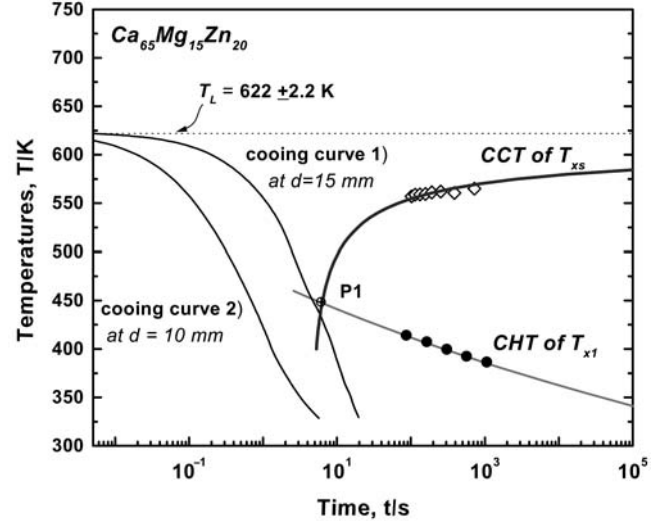


Fig. 5. Calculated CHT curve of T_x versus β by using Eq. 6 and calculated CCT curve by using Eq. 5 for the amorphous $\text{Ca}_{65}\text{Mg}_{15}\text{Zn}_{20}$ alloy together with two cooling curves investigated at different diameters of the ingot.

Fig. 5 shows the calculated integrated transformation curve for $\text{Ca}_{65}\text{Mg}_{15}\text{Zn}_{20}$ alloy together with experimental data from Tables 1 and 2. Also two cooling curves obtained at central axis with different cross sectional diameters of a cone-shaped ingot are included. The cooling curve 2) measured at the center of cross section with a diameter of 10 mm passes away from the apparent nose point P1, indicating that the cooling rate is fast enough to form a glass. The cooling curve 1) measured at the center of cross section with a diameter of 15 mm passes near the apparent nose point P1 without crossing the integrated curve, indicating that the cooling rate is close to a critical cooling rate for glass transition. Also both cooling curves show no recalescence phenomenon, suggesting the suppression of crystalline phase formation. The formation of fully amorphous phase was confirmed by XRD and DSC experiments, as shown in Fig. 6. The alloy specimen with a diameter of 15 mm shows XRD pattern and DSC trace, which are almost same as those from melt spun ribbon specimen. The maximum section size for glass formation in $\text{Ca}_{65}\text{Mg}_{15}\text{Zn}_{20}$ alloy has been reported to be above 15 mm in diameter as listed in Table 3 [5]. The calculated R_c for the $\text{Ca}_{65}\text{Mg}_{15}\text{Zn}_{20}$ alloy was 28 K/s, which is slightly higher than the mean cooling rate of 25 (± 5) K/s from the cooling curve 1). Therefore, the glassy $\text{Ca}_{65}\text{Mg}_{15}\text{Zn}_{20}$ alloy could be formed by casting process with a cooling rate over 28 K/s. This calculated critical cooling rate is in good agreement with previously reported value of 20 K/s [5].

During solidification of $\text{Ca}_{65}\text{Mg}_{15}\text{Zn}_{20}$ alloy, the CaMg_2 phase appears as primary solidification phase if the cooling rate is not high enough to form glass phase [31,32]. In other words, the CaMg_2 phase is competing phase in glass forma-

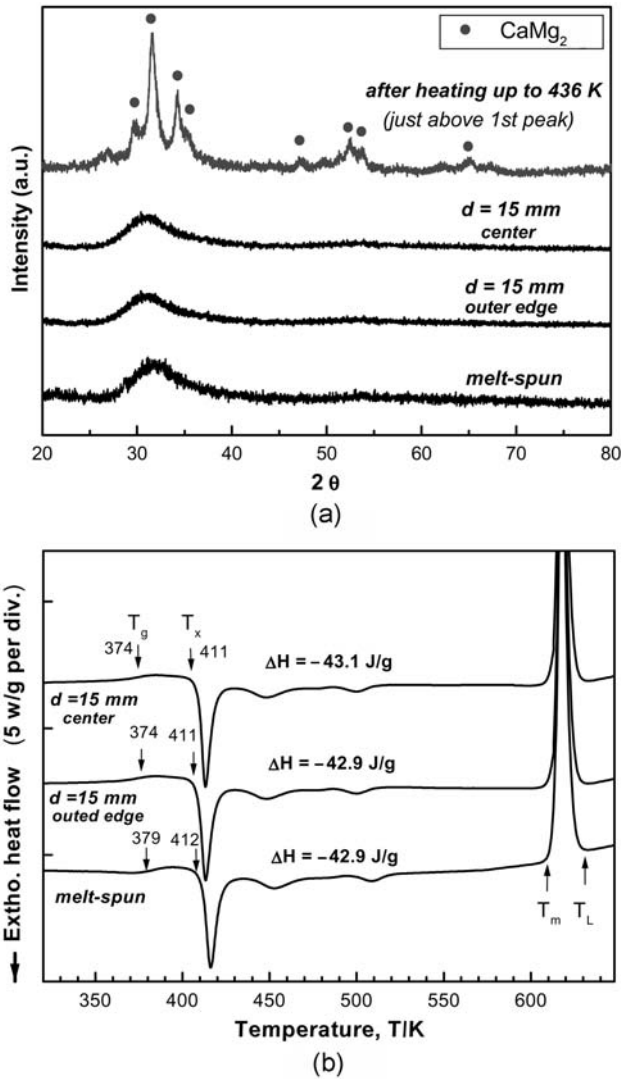


Fig. 6. (a) XRD patterns and (b) DSC traces for the amorphous $\text{Ca}_{65}\text{Mg}_{15}\text{Zn}_{20}$ specimen, melt-spun ribbon and as-cast ingot with a diameter of 15 mm, showing an amorphous nature such as diffuse halo, glass transition and crystallization process. Additionally, XRD pattern taken from the heated specimen up to 436 K is also include.

tion during cooling. Also the same phase forms as a primary phase when the glassy alloy is heated to 436 K, above the first crystallization peak (see Fig. 6(a)). The CaMg_2 phase is a common primary phase during both solidification of liquid and devitrification of metallic glass in $\text{Ca}_{65}\text{Mg}_{15}\text{Zn}_{20}$ alloy.

Therefore, in a view of time-temperature window, the integrated transformation curve gives a boundary between CaMg_2 crystalline phase and undercooled liquid including glassy state and can be considered as an apparent kinetic boundary for the crystallization process of the $\text{Ca}_{65}\text{Mg}_{15}\text{Zn}_{20}$ alloy, even though starting states of the sample on both transformation processes are not identical.

Figs. 7(a)-(d) show calculated integrated transformation curves for $\text{Pd}_{40}\text{Ni}_{10}\text{Cu}_{20}\text{P}_{20}$, Vit1, Vit1a and $\text{Mg}_{65}\text{Cu}_{25}\text{Y}_{10}$ alloys together with corresponding experimental data from Tables 1 and 2. Using these integrated transformation curves, critical cooling rates for glass transition were calculated to be 0.5, 1.7, 6, and 21 K/s for $\text{Pd}_{40}\text{Ni}_{10}\text{Cu}_{20}\text{P}_{20}$, Vit1, Vit1a and $\text{Mg}_{65}\text{Cu}_{25}\text{Y}_{10}$ alloys, respectively. The calculated R_c values are in good agreement with experimentally measured critical cooling rates for corresponding alloys as listed in Table 3. Further quantitative comparison of this model with conventional method has been made. Also critical cooling rate, R_c^* , for glass transition has been calculated from data on cooling rate, a α , dependence of solidification onset temperature T_{xs} using following Eq. 1 (see introduction) [9,10]. R_c^* values calculated from the variation T_{xs} with cooling rate are listed in Table 3. Fig. 8 shows a plot of measured critical cooling rates for $\text{Ca}_{65}\text{Mg}_{15}\text{Zn}_{20}$, $\text{Pd}_{40}\text{Ni}_{10}\text{Cu}_{30}\text{P}_{20}$, Vit1, Vit1a and $\text{Mg}_{65}\text{Cu}_{25}\text{Y}_{10}$, alloys together with critical cooling rates calculated in two different ways (solid symbols (R_c): this model, open symbols (R_c^*): Eq. 1). The values of R_c or R_c^* taken from the amorphous samples in Ca-Mg-Zn (square) and Pd-Ni-Cu-P (circles), Vit1 (down triangle), Vit1a (up triangle) and MgCuY (diamond) alloys. As shown previously the cooling rates calculated from the integrated transformation curve are in good correlation with the measured values for all alloys, while the critical cooling rates from the Eq. 1 are at least one order higher or lower than the measured values except for $\text{Ca}_{65}\text{Mg}_{15}\text{Zn}_{20}$ and Vit1 alloys. The calculated critical cooling rates (R_c and R_c^*) and measured cooling rates for each alloy are listed in Table 3 together with maximum section size (Z_c) for glass transition. These results clearly indicate that the current model gives better agreement with real experimental data than previous method [9,10] in calculating critical cooling rate for glass transition. Further clarification of the application of the model for calculating of R_c in other BMGs having various GFAs is under study.

Table 3. Comparison of critical cooling rates, R_c , for selected BMGs

Alloy (Nominal at.%)	R_c (K/s)	R_c^* (K/s)	Measured R_c (K/s)	Z_c (mm)	Remarks
$\text{Ca}_{65}\text{Mg}_{15}\text{Zn}_{20}$	28	21	24.6±4.9, 20 [4]	>15 [4]	Copper mold cast cone-shaped ingot
$\text{Pd}_{40}\text{Ni}_{10}\text{Cu}_{30}\text{P}_{20}$	0.5	1.0	0.1 [13,19]*, 0.33 [11]	72 [19]	Water quenched rod sample after flux treatment
$\text{Zr}_{41.2}\text{Ti}_{13.8}\text{Cu}_{12.3}\text{Ni}_{10}\text{Be}_{22.5}$ (Vit1)	1.7	1.3	1.4 [1,6]	50 [1]	Copper mold cast sheet
$\text{Zr}_{42.6}\text{Ti}_{12.4}\text{Cu}_{11.3}\text{Ni}_{10}\text{Be}_{23.8}$ (Vit1a)	6	1779	5.0 [6]	-	Copper mold cast sheet
$\text{Mg}_{65}\text{Cu}_{25}\text{Y}_{10}$	22	10	50 [21]	4.0 [20], 7.0 [22]	Copper mold cast cylindrical ingot

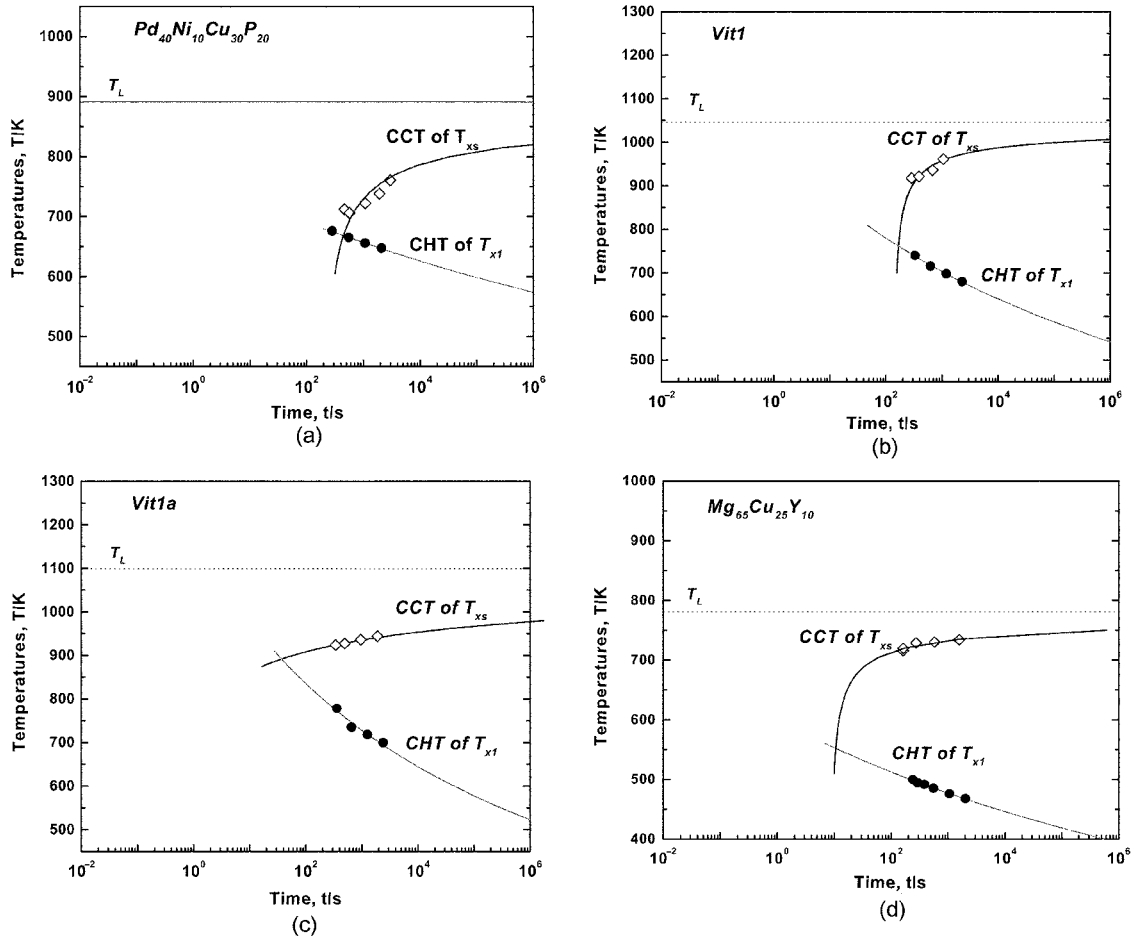


Fig. 7. Calculated CHT curves of T_x versus β by using Eq. 6 and the calculated CCT curves by using Eq. 5 for amorphous alloys: (a) $\text{Pd}_{40}\text{Ni}_{10}\text{Cu}_{30}\text{P}_{20}$, (b) $\text{Zr}_{41.2}\text{Ti}_{13.8}\text{Cu}_{12.5}\text{Ni}_{10}\text{Be}_{22.5}$, (c) $\text{Zr}_{42.6}\text{Ti}_{12.4}\text{Cu}_{11.3}\text{Ni}_{10}\text{Be}_{23.8}$, and (d) $\text{Mg}_{65}\text{Cu}_{25}\text{Y}_{10}$.

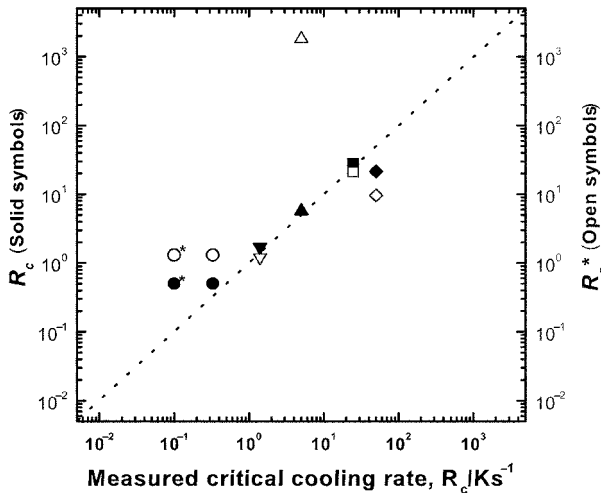


Fig. 8. Critical cooling rates, R_c (solid symbols) derived from integrated transformation kinetics from CCT curves with CHT curves in terms of the directly measured value for Ca-Mg-Zn alloy (square) and the previously reported values for Pd-Ni-Cu-P [11,13,19] (circles), Vit1 [6] (down triangle), Vit1a [6] (up triangle) and Mg-Cu-Y [21] (diamond). For more comparison, the derived values of R_c^* through the Eq. 1 are also marked as open symbols. Here, * marks of cycle were presented by different reported values for $\text{Pd}_{40}\text{Ni}_{10}\text{Cu}_{30}\text{P}_{20}$ (see Table 3).

4. CONCLUSIONS

A semi-empirical model to estimate a critical cooling rate (R_c) for glass formation from thermal analysis data has been developed. An integrated transformation curve was constructed by combining continuous cooling transformation (CCT) curve and continuous heating transformation (CHT) curve. Using classical nucleation kinetics, the CCT curve was calculated from the variation of solidification onset temperature with cooling rate during continuous cooling of liquid. Using Kissinger method, the CHT curve was calculated from the variation of crystallization onset temperature with heating rate during continuous heating of glass specimen. Critical cooling rate was calculated from the intersection point of the two curves, corresponding to an apparent nose point in the integrated transformation curve. The calculated R_c s were 0.5, 1.7, 6, 21, and 28 K/s for $\text{Pd}_{40}\text{Ni}_{10}\text{Cu}_{30}\text{P}_{20}$, $\text{Zr}_{41.2}\text{Ti}_{13.8}\text{Cu}_{12.5}\text{Ni}_{10}\text{Be}_{22.5}$, $\text{Zr}_{42.6}\text{Ti}_{12.4}\text{Cu}_{11.3}\text{Ni}_{10}\text{Be}_{23.8}$, $\text{Mg}_{65}\text{Cu}_{25}\text{Y}_{10}$ and $\text{Ca}_{65}\text{Mg}_{15}\text{Zn}_{20}$ alloys, respectively. The calculated critical cooling rate was in good agreement with measured value for the alloys. The current model shows a better agreement with

experimental measurements than conventional method.

ACKNOWLEDGMENTS

The authors are grateful for the financial support of the Creative Research Initiatives of the Korean Ministry of Science and Technology. W.T. Kim also thanks for the financial support from the Center for Advanced Materials Processing (CAMP) of the 21st Century Frontier R&D Program funded by the Ministry of Science and Technology, Republic of Korea.

REFERENCES

1. Z. P. Lu and C. T. Liu, *Acta mater.* **50**, 3501 (2002).
2. A. Inoue, *Acta mater.* **48**, 279 (2000).
3. Z. P. Lu and C. T. Liu, *Phys. Rev. Lett.* **91**, 115 (2003).
4. W. B. Kim, B. J. Ye, and S. Yi, *Met. Mater. -Int.* **10**, 1 (2004).
5. E. S. Park and D. H. Kim, *J. Mater. Res.* **19**, 685 (2004).
6. J. Y. Lee, D. H. Bae, J. K. Lee, and D. H. Kim, *J. Mater. Res.* **19**, 2221 (2004).
7. T. A. Waniuk, J. Schoers, and W. L. Johnson, *Appl. Phys. Lett.* **78**, 1213 (2001).
8. D. R. Uhlmann, *J. Non-Cryst. Solids* **7**, 337 (1972).
9. J. M. Barandiaran and J. Colmenero, *J. Non-Cryst. Solids* **46**, 277 (1981).
10. A. Inoue, T. Zang, and T. Masumoto, *J. Non-Cryst. Solids* **156-158**, 473 (1993).
11. D. M. Herlach, *Mater. Sci. & Eng. R* **12**, 177 (1994).
12. J. F. Löffler, J. Schroers, and W. L. Johnson, *Appl. Phys. Lett.* **77**, 681 (2000).
13. F. Gillessen, *Ph. D. Thesis*, Ruhr-University Bochum, Germany (1989).
14. N. Nishiyama and A. Inoue, *Acta mater.* **47**, 1487 (1999).
15. X. H. Lin and W. L. Johnson, *J. Appl. Phys.* **78**, 6514 (1995).
16. J. -H. Kim, S. G. Kim, and A. Inoue, *Acta mater.* **49**, 615 (2001).
17. P. I. K. Onorato and D. R. Uhlmann, *J. Non-Cryst. Solids* **22**, 367 (1976).
18. D. V. Louzguine and A. Inoue, *Appl. Phys. Lett.* **81**, 2561 (2002).
19. H. A. Davies, *Phys. Chem. Glasses* **17**, 159 (1976).
20. N. Nishiyama and A. Inoue, *Mater. Trans., JIM* **38**, 464 (1997).
21. A. Inoue, A. Kato, T. Zhang, S. G. Kim, and T. Masumoto, *Mater. Trans., JIM* **32**, 609 (1991).
22. R. Busch, W. Liu, and W. L. Johnson, *J. Appl. Phys.* **83**, 4134 (1998).
23. A. Inoue, T. Nakamura, N. Nishiyama, and T. Masumoto, *Mater. Trans., JIM* **33**, 937 (1992).
24. R. I. Wu and J. H. Perepezko, *Metall. Mater. Trans. A* **31**, 497 (2000).
25. D. Turnbull, *J. Appl. Phys.* **21**, 1022 (1950).
26. C. V. Thompson and F. Spaepen, *Acta mater.* **27**, 1855 (1979).
27. K. Mondal, U. K. Chatterjee, and B. S. Murty, *Appl. Phys. Lett.* **83**, 671 (2003).
28. H. E. Kissinger, *J. Res. Natl. Bur. Stand. Sect. A* **57**, 217 (1956).
29. L. C. Chen and F. Spaepen, *J. Appl. Phys.* **69**, 679 (1991).
30. D. V. Louzguine and A. Inoue, *Scripta mater.* **47**, 887 (2002).
31. P. Villars, A. Prince, and H. Okamoto, Handbook of ternary alloy phase diagrams **6**, 7522 (1995).
32. E. S. Park and D. H. Kim, Submitted to *J. Non-Cryst. Solid*.